Journal of Computational Physics **183,** 165–186 (2002)
doi:10.1006/jcph.2002.7187

A Highly Accurate Technique for the Treatment of Flow Equations at the Polar Axis in Cylindrical Coordinates Using Series Expansions

G. S. Constantinescu and S. K. Lele

Center for Turbulence Research, Department of Mechanical Engineering,
Stanford University, Stanford, California 94305-3030
E-mail: gconstan@ctr.stanford.edu and lele@leland.stanford.edu

Received August 13, 2001; revised August 5, 2002

Numerical methods for solving the flow equations in cylindrical or spherical coordinates should be able to capture the behavior of the exact solution near the regions where the particular form of the governing equations is singular. In this work we focus on the treatment of these numerical singularities for finite-difference methods by reinterpreting the regularity conditions developed in the context of pseudospectral methods. A generally applicable numerical method for treating the singularities present at the polar axis, when nonaxisymmetric flows are solved in cylindrical coordinates using highly accurate finite-difference schemes (e.g., Pade schemes) on nonstaggered grids, is presented. Governing equations for the flow at the polar axis are derived using series expansions near $r = 0$. The only information needed to calculate the coefficients in these equations are the values of the flow variables and their radial derivatives at the previous iteration (or time) level. These derivatives, which are multivalued at the polar axis, are calculated without dropping the accuracy of the numerical method using a mapping of the flow domain from $(0, R) * (0, 2\pi)$ to $(-R, R) * (0, \pi)$, where R is the radius of the computational domain. This allows the radial derivatives to be evaluated using high-order differencing schemes (e.g., compact schemes) at points located on the polar axis. The accuracy of the method is checked by comparison with the theoretical solution corresponding to a circular compressible forced jet in the regime of linear growth. The proposed technique is illustrated by results from simulations of laminar-forced jets and turbulent compressible jets using large eddy simulation (LES) methods. In terms of the general robustness of the numerical method and smoothness of the solution close to the polar axis, the present results compare very favorably to similar calculations in which the equations are solved in Cartesian coordinates at the polar axis, or in which the singularity is removed by employing a staggered mesh in the radial direction without a mesh point at $r = 0$, following the method proposed recently by Mohseni and

0021-9991/02 $35.00

Colonius [1]. Extension of the method described here for incompressible flows or for any other set of equations that is solved on a nonstaggered mesh in cylindrical or spherical coordinates with finite-difference schemes of various levels of accuracy is immediate.

Key Words: coordinate system singularity; polar axis; turbulence; large eddy simulation method; cylindrical system; collocated grids; finite differences method.

---

1. BACKGROUND

The singularities at the centerline of a cylindrical coordinate system are due to the presence of terms containing the factor $1/r$, where r is the radial distance, in the equations governing the flow. The flow field itself does not have any singularity at the polar axis. For axisymmetric flows symmetry conditions may be used to remove these singularities, but in the simulation of nonaxisymmetric flows this problem must be faced. Furthermore, as the computational domain is defined as $(0, 2\pi) * (0, R)$, one has to specify numerical boundary conditions at $r = 0$, even if physically there is no boundary at the polar axis.

Several numerical methods have been proposed to address the singularity of the flow equations in cylindrical or spherical coordinates. At first sight they seem to vary greatly depending on whether a pseudo-spectral, finite-volume, or finite-difference framework is adopted, but in fact there are many similarities among them. This is especially true for the new finite-difference method on nonstaggered grids proposed here and the treatment used with pseudo-spectral methods. There are also common elements with methods that use l'Hopital's rule [2] or that use a "shifted" distribution of points in the radial direction [1] to eliminate the points on the polar axis.

The main idea behind using spectral methods in cylindrical coordinates is to seek an approximation using polynomial expansions in the radial direction that satisfy some regularity conditions so as to insure a well-behaved solution near the polar axis. O'Sullivan and Breuer [3] studied the growth of linear disturbances in pipe flow. They solved the Navier–Stokes equations using Fourier transforms in both the streamwise and the azimuthal directions, and Chebyshev polynomials in the radial direction. The singularity at the polar axis was avoided by using information in wavenumber space related to the form of the series expansions of the velocity and pressure variables at $r = 0$, and by mapping in the radial direction to increase resolution near the polar axis. Orszag and Patera [4], in a related study, used a similar spectral method but they employed parity relations for the Chebyshev coefficients in the expansions to remove the coordinate singularity of the cylindrical system. Fully developed pipe-flow DNS calculations in cylindrical coordinates using spectral methods were reported in [5, 6]. The method in [5] used Jacobi polynomials as the expansion basis in the radial direction close to the polar axis and Legendre–Lagrangian interpolants away from the axis, while the latter used B-spline polynomials expansions. An adaptation of the method proposed in [5] for spherical coordinates, where one is faced with essentially the same problem at the two singularity axes corresponding to polar angles $\varphi = 0$ and $\varphi = \pi$, can be found in [7]. Zhang *et al.* [5] were able to recast the governing system of equations in the wavenumber space so that the singularities due to coefficients of the form $1/r$ and $1/r^2$ were removed. This was essentially done by taking advantage of the particular form of the series expansions in wavenumber space of the pressure and velocity components. However, they still had to use a special form of Jacobi polynomials in the radial direction close to the origin in conjunction with l'Hopital's rule to remove potential singularities arising because of terms where both the numerator and the denominator tend to zero at approximately the same rate near the polar axis. Loulou [6] followed a similar approach, but the regularity conditions in terms of having a certain behavior in r near the origin in the polynomial expansions of the Fourier modes were imposed as constraints on the coefficients of the B-splines. These regularity conditions are essentially the same ones we are going to use in our method, but in the present work everything is formulated in the physical space (r, θ, z) as opposed to wavenumber space (r, k_θ, k_z). In the spectral methods the essential information is the order of the leading term in the polynomial expansions in r for each mode of the Fourier expansion in θ. No explicit equations at the polar axis are derived, and there is no need to calculate the values of the coefficients in these expansions. Finally, a somewhat different approach was proposed in [8] in the context of pseudo-spectral (interpolatory) methods. By use of the governing differential equations, pole conditions were derived in [8] which were subsequently used as numerical boundary conditions at the coordinate singularity. The advantage of the method is that these pole conditions are developed in physical space and are easier to implement into a standard pseudo-spectral method. The method was illustrated for solving a Poisson equation on the unit disk.

Finite-volume and finite-difference methods are less accurate than spectral methods, but they can handle complex geometrical configurations more easily. Finite-volume methods for flows in cylindrical geometries were employed by Eggels *et al.* [9], Akselvoll and Moin [10, 11], and Boersma *et al.* [12], among others. The main difficulty here is related to the fact that the azimuthal and streamwise fluxes are not defined at the centerline. Due to the definition of velocity components at the center of the volume cells, the singularity for the azimuthal and streamwise fluxes is removed. However, if the control volume closest to the centerline is not wedge shaped, the flux at the first control-volume surface off the polar axis whose normal is oriented in the radial direction must be evaluated. In one of the implementations of their numerical method, Eggels *et al.* [9] used first- and second-order one-sided differences to extrapolate the radial velocity on the faces closest to the centerline. A similar procedure was used to calculate the diffusive flux at these locations. Loss of accuracy near $r = 0$ was found to be not very significant due to the relatively smooth DNS velocity fields in that region for the pipe flow. They also tried to use wedge-shaped elements at the centerline, the advantage being that the singularity is automatically removed as the radial flux is identically equal to zero on the faces "located" at the centerline. In this implementation the method was found to give unrealistically high values for the r.m.s. fluctuations near the centerline. However, one should point out that Boersma *et al.* [12], using a similar method, did not observed such problems in their DNS simulations of incompressible jets. Akselvoll and Moin [10] used a finite-volume method to solve for the turbulent flow in a coaxial jet combustor using LES. They used regular-shaped elements near the centerline, with the closest faces located at $\Delta r/2$ from the singularity axis. Provided the radial and azimuthal velocity components u_r and u_θ are well defined at the centerline for all θ's (they are multivalued at $r = 0$), the calculation of the fluxes on these faces presents no special problem. They interpolated the values for the radial velocity at every azimuthal location θ on the centerline using the corresponding values at $\Delta r/2$ for two azimuthal angles, θ and $\theta + \pi$, and accounting for the change in sign for the radial velocity across the centerline in the limit $r \to 0$. A similar treatment was followed for the azimuthal velocity at the centerline that was needed to compute some viscous fluxes in the momentum equation for the azimuthal fluxes.

Verzicco and Orlandi [13] developed a second-order finite-difference scheme in cylindrical coordinates. The main feature of their method was the introduction of a radial flux (ru_r) on a staggered grid. As for finite-volume methods, this is the only flux to be calculated right at $r = 0$, and its value there is obviously equal to zero. The DNS study in [14] used this algorithm to calculate the fully turbulent flow in pipes with rotating walls. Their method seems to be very appealing in the context of second-order schemes, but extension to higher order schemes is not straightforward.

Griffin *et al.* [2] used finite differences and L'Hopital's rule to recast the governing equations at the origin. For all terms involving coordinate singularities they calculated the radial derivatives using one-sided second-order-accurate finite differences, while the azimuthal derivatives for the variables that are multivalued at the origin were formally evaluated by using the values at neighboring azimuthal locations and $\Delta\theta = 2\pi/N_\theta$, where N_θ is the number of cells in the azimuthal direction. This resulted in a set of new equations at the origin that do not contain any singularities. Formally this treatment was not very rigorous, as all these values are physically located at the same point, but the second-order method was found to produce smooth solutions near the polar axis at least in the framework of the inviscid calculation of the I.C. engine that they considered. However, its use for DNS or LES simulations using higher order schemes is doubtful, and in the next section we discuss in a more rigorous way using series expansions the errors introduced by the use of L'Hopital's rule to remove the singularities at the polar axis. This will also answer the question which they raised in their paper about whether or not a fixed limit exists for terms like $(1/r)\partial p/\partial\theta$, which using l'Hopital's rule they recast into $\partial^2 p/\partial r\partial\theta$. We show that in this case such a limit exits and can be written using Fourier series expansions of the pressure in terms of the $m = 1$ and $m = -1$ modes (the pressure cross derivative is multivalued at the origin). For this particular example the Fourier expansions of $1/r\partial p/\partial\theta$ and $\partial^2 p/\partial r\partial\theta$ give the same limit; however, we also show other examples (e.g., the Laplacian operator that is present in the viscous term) where these kinds of approximations using l'Hopital's rule will lead to a wrong result.

Finally, Mitchell *et al.* [15], Freund [16], and Boersma and Lele [17] used compact finite differences on nonstaggered meshes in cylindrical coordinates to compute the radiated jet noise of compressible jets. In these studies, the equations at the polar axis were solved using a Cartesian coordinate system. The directions of the Cartesian system were arbitrarily chosen, and the multivalued variables (u_r, u_θ) for the other directions were obtained by rotation of the system at $r = 0$, where only modes $m = 1$ and $m = -1$ may exist. As the present numerical scheme is very similar to the ones used in these studies, more details can be found in the validation section. Another option for removing the singularities at the polar axis is to eliminate the points at $r = 0$ by distributing the points in the radial direction starting with $\Delta r/2$ (for a uniform grid spacing in r) and mapping the domain $(0, 2\pi) * (0, R)$ into $(0, \pi) * (-R, R)$ for evaluating the radial derivatives. This ensures that no numerical boundary conditions have to be specified at the polar axis. The radial derivative stencils will span the centerline without evaluation at $r = 0$. This is essentially the method discussed in [1]. We use this idea but recast it for the case in which we have points at the polar axis. As we derive a set of exact equations which are well defined on the polar axis, we do not have to avoid the presence of such points at the centerline.

2. TREATMENT OF THE EQUATIONS AT THE POLAR AXIS

Let us suppose that the system of governing equations may be written as

$$\frac{\partial Q}{\partial t} = \mathrm{RHS}(Q), \tag{1}$$

where, for instance, in the case of compressible three-dimensional flows, $Q = (\rho u_x, \rho u_r, \rho u_\theta, \rho, e)$, ρ is the density, e is the energy, and the right-hand-side term (RHS) contains the usual operators in cylindrical coordinates associated with the continuity or the transport equations of momentum and energy, including the terms associated with the subgrid scale contributions in the case of LES simulations.

The numerical method is general enough that the particular form of the operators in the RHS is not really important. The same is true if more equations are included in Eq. (1), such as transport equations for passive scalars, or for turbulence quantities in the case of RANS calculations. The only important difference between the different equations in Eq. (1) is determined by whether the variable in the left hand side of Eq. (1) is single valued or multivalued at the polar axis. Following Boyd [19], the most general expansion of any function that is not multivalued at the polar axis (scalars, pressure, streamwise velocity) can be written as

$$F(r,\theta) = \sum_{m=0}^{\infty} (f_m(r) \cdot \cos(m\theta) + g_m(r) \cdot \sin(m\theta)), \tag{2}$$

where f_m and g_m are polynomials in r that have mth-order zeroes at $r = 0$. If m is even, f_m and g_m are both symmetric around $r = 0$ and their power series contain only even powers of r, while if m is odd, f_m and g_m are both antisymmetric and accordingly their power series contain only odd powers of r. A similar statement holds for ru_r and ru_θ, which takes care of the expansion form for multivalued variables at the origin. These conditions imply that the most general series expansion of a single-valued quantity (S) at the polar axis can be written as

$$S(r,\theta) = \sum_{m=0}^{\infty} r^m \left(\sum_{n=0}^{\infty} \alpha_{mn} r^{2n} \right) \cdot \cos(m\theta) + \sum_{m=0}^{\infty} r^m \left(\sum_{n=0}^{\infty} \beta_{mn} r^{2n} \right) \cdot \sin(m\theta), \tag{3}$$

while the expressions for multivalued quantities (e.g., u_r and u_θ) assume the form

$$\begin{aligned} M(r,\theta) = {} & \frac{1}{r} \sum_{n=1}^{\infty} A_{0n} r^{2n} + \sum_{m=1}^{\infty} r^{m-1} \left(\sum_{n=0}^{\infty} A_{mn} r^{2n} \right) \cdot \cos(m\theta) \\ & + \sum_{m=1}^{\infty} r^{m-1} \left(\sum_{n=0}^{\infty} B_{mn} r^{2n} \right) \cdot \sin(m\theta). \end{aligned} \tag{4}$$

A sketch of the proof of Eq. (3) can be given, starting with the most general Fourier expansion of S in the form of Eq. (2) and requiring that all terms be regular at the origin. The Fourier expansion in terms of complex variables can be written as

$$F(r,\theta) = \sum_{m=0}^{\infty} (\hat{f}_m(r) e^{im\theta}), \tag{5}$$

where $\hat{f}_m(r)$ is a polynomial in r with complex coefficients. Each term in the summation can be written as

$$\hat{f}_m(r)e^{im\theta} = \sum_{n=0}^{\infty} c_n(m)r^n e^{im\theta} = r^m e^{im\theta} \sum_{n=0}^{\infty} c_n(m)r^{n-m} = w^m \sum_{n=0}^{\infty} c_n(m)r^{n-m}, \quad (6)$$

where $w = y + iz = re^{i\theta}$. As w^m is regular at origin for all $m \geq 0$, the requirement that each term in Eq. (5) be regular implies $c_n(m) = 0$ for $n < m$, as $1/r^s$ is not regular at origin for $s > 0$. Also $r^s = (\sqrt{(y^2 + z^2)})^s$ is regular only for even values of s. For odd values of s the derivative of r^s with respect to y or z will contain $1/\sqrt{r}$, which is not analytic at origin.

The form of the series expansions for multivalued quantities (e.g., for u_r) can be deduced by observing that u_r can be written in terms of the Cartesian velocity components u_y and u_z as

$$u_r = u_y \cos(\theta) + u_z \sin(\theta), \quad (7)$$

where the form of u_y and u_z expansions is given by (3). By regrouping the terms and using algebraic identities of the form $2\cos(\theta)\cos(m\theta) = \cos((m-1)\theta) + \cos((m+1)\theta)$, one can easily recover Eq. (4).

As we previously mentioned, any scalar or Cartesian velocity component is uniquely defined at the origin, so one can write

$$\left.\frac{\partial S}{\partial \theta}\right|_{r=0} = 0. \quad (8)$$

This relation holds in particular for $u_z = u_r \sin(\theta) + u_\theta \cos(\theta)$. So by taking the derivatives with respect to θ one can write

$$0 = \left.\left(\frac{\partial u_r}{\partial \theta} - u_\theta\right)\right|_{r=0} \sin(\theta) + \left.\left(\frac{\partial u_\theta}{\partial \theta} + u_r\right)\right|_{r=0} \cos(\theta). \quad (9)$$

As Eq. (9) should hold for any θ, one obtains

$$\frac{\partial u_r}{\partial \theta} = u_\theta \quad \text{and} \quad \frac{\partial u_\theta}{\partial \theta} = -u_r \quad \text{at } r = 0. \quad (10)$$

There is another important constraint on the general form of the series expansions for u_r and u_θ. If $A_{ij}^{(r)}$, $B_{ij}^{(r)}$, $A_{ij}^{(\theta)}$, and $B_{ij}^{(\theta)}$ are the coefficients of the series expansions for u_r and u_θ in Eq. (4), the following relation holds for all $i \geq 1$:

$$A_{i0}^{(\theta)} = B_{i0}^{(r)} \quad \text{and} \quad B_{i0}^{(\theta)} = -A_{i0}^{(r)}. \quad (11)$$

This relation can be obtained by using the corresponding series expansions given by Eq. (3) for u_y and by Eq. (4) for u_r and u_θ, respectively. These series expansions are plugged into

$$u_y = u_r \cos(\theta) - u_\theta \sin(\theta), \quad (12)$$

and using algebraic identities similar to the ones employed to deduce the general form of the series expansions for multivalued variables at the polar axis (Eq. (4)), one can see that the polynomial multiplying cos(2θ) in the RHS of Eq. (12) has the form

$$\frac{1}{2}\left(B_{10}^{(\theta)} + A_{10}^{(r)} + r^2(\cdots) + \cdots\right). \tag{13}$$

As this polynomial should have a double zero at the origin, one should require $B_{10}^{(\theta)} = -A_{10}^{(r)}$. The other relations in Eq. (11) follow similarly from analysis of the form of polynomials multiplying the other modes in the RHS of Eq. (12).

By calculating the derivatives with respect to θ and r of the series expansions given by Eqs. (3) and (4) for all operators present in the RHS of the governing equations Eq. (1), and taking the limit $r \to 0$, a new form of the governing equations that is valid at $r = 0$ is obtained. These are a set of exact equations at the polar axis, provided we can calculate exactly the coefficients $A_{mm}, B_{mn}, \alpha_{mn}, \beta_{mn}$ for all terms present in the RHS of Eq. (1). However, for a system of PDEs with second-order radial derivatives, as is the case for the Navier–Stokes equations, it is sufficient to calculate at most the coefficients whose indices m and n vary between 0 and 2, as we show next. The final expressions in the RHS of Eq. (1) are dependent on the particular set of equations that is solved (inviscid, laminar, turbulent, compressible, incompressible, etc.). However, the present method is valid for any system of equations that can be written in cylindrical (or spherical) coordinates in the form of Eq. (1). Hence, reference is made to the Appendix for the final expression of the RHS corresponding to the compressible turbulent flow equations that were used in the present flow calculations to validate this method. In the following discussion we focus our attention on pointing out some general features.

At this point it is relevant to look at the expressions for the series expansions of a single-valued variable at the origin, let us say the streamwise velocity u_x (coefficients in series expansions are labeled $\alpha_{mn}^{(x)}$ and $\beta_{mn}^{(x)}$), and for a multivalued one, the radial velocity u_r (coefficients are $A_{mn}^{(r)}$ and $B_{mn}^{(r)}$), as well as their first and second radial derivatives, in the limit $r \to 0$:

$$u_x = \alpha_{00}^{(x)}, \tag{14}$$

$$\frac{\partial u_x}{\partial r} = \alpha_{10}^{(x)}\cos(\theta) + \beta_{10}^{(x)}\sin(\theta), \tag{15}$$

$$\frac{\partial^2 u_x}{\partial r^2} = 2\alpha_{01}^{(x)} + 2\alpha_{20}^{(x)}\cos(2\theta) + 2\beta_{20}^{(x)}\sin(2\theta), \tag{16}$$

$$u_r = A_{10}^{(r)}\cos(\theta) + B_{10}^{(r)}\sin(\theta), \tag{17}$$

$$\frac{\partial u_r}{\partial r} = A_{10}^{(r)} + A_{20}^{(r)}\cos(2\theta) + B_{20}^{(r)}\sin(2\theta), \tag{18}$$

$$\frac{\partial^2 u_r}{\partial r^2} = 2A_{11}^{(r)}\cos(\theta) + 2B_{11}^{(r)}\sin(\theta) + 2A_{30}^{(r)}\cos(3\theta) + 2B_{30}^{(r)}\sin(3\theta). \tag{19}$$

As expected the series expansions of scalar quantities (e.g., u_x) contain only the $m = 0$ mode, while those of u_r and u_θ contain only the $m = 1(\cos(\theta))$ and $m = -1(\sin(\theta))$ modes. Meanwhile, the first derivative of a scalar quantity is multivalued, as it contains the $m = 1$ and -1 modes, while the second derivative contains the $m = 0, 2$, and -2 modes. In particular, this applies to the pressure, p, which is a single-valued scalar, but $\partial p/\partial r$ is multivalued at $r = 0$. If we go back to Eq. (1) for the u_x variable, and if we take the limit as $r \to 0$, we obtain

$$\frac{\partial u_x}{\partial t} = \frac{\partial \alpha_{00}^{(x)}}{\partial t} = \mathrm{RHS}_{u_x}, \tag{20}$$

where RHS_{u_x} contains terms coming from the convective and viscous operators that would obviously involve modes $m = 0, 1, -1, 2, -2, 3$, and -3 (see the Appendix). In order for Eq. (20) to be valid, the coefficients resulting from the series expansions of the different variables and their derivatives should be such that the coefficients multiplying all but the $m = 0$ mode in RHS_{u_x} must be equal to zero. Indeed this is what happens when we sum the contributions coming from all the terms contained in RHS_{u_x} and use Eq. (11). However, individual terms may contain nonzero coefficients multiplying the $m \neq 0$ modes. In fact, it can be proven that this property holds not only for the RHS of the equations describing the transport of a single-valued variable at the polar axis as a whole, but also for independent operators such as convective, viscous, dilatation, and viscous dissipation in the energy equation. For instance, the dilatation operator, which is a scalar quantity and thus should contain only the $m = 0$ mode, can be expressed as

$$\frac{\partial u_x}{\partial x} + \frac{\partial u_r}{\partial r} + \frac{1}{r}\left(u_r + \frac{\partial u_\theta}{\partial \theta}\right) = \frac{\partial \alpha_{00}^{(x)}}{\partial x} + 2A_{01}^{(r)}, \tag{21}$$

where the streamwise derivative can be calculated with exactly the same method used (sixth-order compact differences in the present work) for points situated away from the polar axis. The same observation is true for the continuity equation, recast as an evolution equation for the density:

$$\frac{\partial \rho}{\partial t} = -\left(\frac{\partial \rho u_x}{\partial x} + \frac{1}{r}\frac{\partial r\rho u_r}{\partial r} + \frac{1}{r}\frac{\partial \rho u_\theta}{\partial \theta}\right) = -\left(\frac{\partial \alpha_{00}^{(\rho)}\alpha_{00}^{(x)}}{\partial x} + A_{10}^{(r)}\alpha_{10}^{(\rho)} + B_{10}^{(r)}\beta_{10}^{(\rho)} + 2A_{01}^{(r)}\alpha_{00}^{(\rho)}\right). \tag{22}$$

In Eq. (22) the series coefficients for the density ρ are $\alpha_{mn}^{(\rho)}$ and $\beta_{mn}^{(\rho)}$. Another example is the Laplacian operator (e.g., the viscous term in the u_x-momentum equation, or more exactly the term corresponding to the constant viscosity part):

$$\frac{\partial^2 u_x}{\partial x^2} + \frac{\partial^2 u_x}{\partial r^2} + \frac{1}{r}\frac{\partial u_x}{\partial r} + \frac{1}{r^2}\frac{\partial^2 u_x}{\partial \theta^2} = \frac{\partial^2 \alpha_{00}^{(x)}}{\partial x^2} + 4\alpha_{01}^{(x)}. \tag{23}$$

For the u_r- and u_θ-momentum equations the RHS will contain only the $m = -1$ and $m = 1$ modes once contributions from all the terms are added. These two equations are identical in the limit $r \to 0$; thus it is sufficient to calculate the limit for only one of the equations, e.g.,

$$\frac{\partial u_r}{\partial t} = \frac{\partial A_{10}^{(r)}\cos(\theta) + B_{10}^{(r)}\sin(\theta)}{\partial t} = \mathrm{RHS}_{u_r} = \mathrm{RHS}^{m=1}\cos(\theta) + \mathrm{RHS}^{m=-1}\sin(\theta). \tag{24}$$

In fact, we will end up with two scalar equations, corresponding to the $m = 1$ and -1 modes, respectively, as one can see from the previous relation, the reason being that as $r \to 0$, u_r can be obtained from u_θ by a counterclockwise rotation of $\pi/2$. This means that if the radial component at the polar axis is given by Eq. (17), the azimuthal component can be written as

$$u_\theta = A_{10}^{(\theta)}\cos(\theta) + B_{10}^{(\theta)}\sin(\theta) = -A_{10}^{(r)}\sin(\theta) + B_{10}^{(r)}\cos(\theta), \tag{25}$$

where use was made of relation (11). Relation (23) can also be used to show an inherent problem with methods in which l'Hopital's rule is applied numerically to remove singularities at the polar axis (e.g., [2]). In these methods the Laplacian will be calculated at the polar axis by numerically evaluating the expression

$$\frac{\partial^2 u_x}{\partial x^2} + \frac{\partial^2 u_x}{\partial r^2} + \frac{\partial^2 u_x}{\partial r^2} + \frac{\partial^2}{\partial r^2}\left(\frac{\partial^2 u_x}{\partial \theta^2}\right) = \frac{\partial^2 \alpha_{00}^{(x)}}{\partial x^2} + 4\alpha_{01}^{(x)} - 4\alpha_{20}^{(x)}\cos(2\theta) - 4\beta_{20}^{(x)}\sin(2\theta), \tag{26}$$

which introduces a finite error, as the coefficients of the $m = 2$ and $m = -2$ modes are now present.

The last step needed to complete the presentation of the present method is to describe how the asymptotic series coefficients that are needed to evaluate the RHS in Eq. (1) are computed. We will show that all that is required to calculate these coefficients accurately is to be able to estimate numerically the first- and second-order radial derivatives of all the variables in RHS with the same order of accuracy as points away from the polar axis. In particular, in our compressible flow solver we use sixth-order Pade schemes to calculate the radial derivatives. To do this, the following algorithm, similar to the one used in [1], is adopted. The computational domain is mapped at every $x =$ constant, such as there is no need to specify numerical boundary conditions at $r = 0$. The mapping function $(r, \theta) \rightarrow (\hat{r}, \hat{\theta})$ is

$$\begin{cases} \hat{r} = r \\ \hat{\theta} = \theta \end{cases} \text{for } \begin{matrix} 0 < \theta < \pi, \\ 0 < r < R, \end{matrix} \quad \text{and} \quad \begin{cases} \hat{r} = -r \\ \hat{\theta} = \theta - \pi \end{cases} \text{for } \begin{matrix} \pi < \theta < 2\pi, \\ 0 < r < R. \end{matrix} \tag{27}$$

All variables are identical in both systems of coordinates for $0 < \theta < \pi$. The rules concerning the sign changes for the different variables and operators in the subdomain defined by $0 < r < R$ and $\pi < \theta < 2\pi$ follow from Eq. (27):

$$\begin{aligned} u_{\hat{r}} &= \frac{d\hat{r}}{d\tau} = -\frac{dr}{d\tau} = -u_r, \\ u_{\hat{\theta}} &= \frac{\hat{r}d\hat{\theta}}{d\tau} = -\frac{rd\theta}{d\tau} = -u_\theta, \\ \frac{\partial}{\partial \hat{r}} &= -\frac{\partial}{\partial r}, \quad \frac{\partial}{\partial \hat{\theta}} = \frac{\partial}{\partial \theta}, \quad \text{and} \quad \hat{s} = s \text{ for any scalar variable } s. \end{aligned} \tag{28}$$

As all the signs of scalar quantities and streamwise velocities are left unchanged by the mapping, Eq. (28) is sufficient to determine the sign of all terms involving radial derivatives in the RHS of Eq. (1) in the mapped domain. The radial derivatives are now taken from $-R$ to R, with $r = 0$ being a regular interior point instead of a "numerical" boundary point. For example, before taking the radial derivative of $(r\rho u_\theta u_r)$, which appears in the u_θ-momentum equation, one has to multiply the values for $\theta = (\pi, 2\pi)$ by -1, because of the three changes of sign (for r, u_θ, and u_r) required by the mapping. One should point out that even if a scalar quantity is single valued at origin, its radial derivative is not. Once the radial derivatives are calculated, the inverse transformation of Eq. (28) is taken, so the azimuthal and streamwise derivatives are estimated with the usual coordinate definition $(0, R) * (0, 2\pi)$.

Next, we expand on the calculation of the required coefficients in the asymptotic expansions for u_r, and its radial derivatives. All other variables are treated in a similar fashion using the appropriate series expansions. Suppose that $N_\theta + 1$ is the number of points in the azimuthal direction (with modes $0, \pm 1, \pm 2, \ldots, \pm N_\theta/2$). According to Eq. (17), only the $m = 1$ and -1 modes should be present in a series formed by these N_θ values. We will formally associate the N_θ values with θ, going from $0(N_\theta = 1)$ to $2\pi(N_\theta + 1)$. A fast Fourier transform can, in principle, be applied and the coefficients of the $m = \pm 1$ modes will be $A_{10}^{(r)}$ and $B_{10}^{(r)}$; the other coefficients should be very small. This can also be done for the first and second radial derivatives using their asymptotic expansions in Eqs. (18) and (19) to find $A_{01}^{(r)}$, $A_{20}^{(r)}$, $B_{20}^{(r)}$, and $A_{11}^{(r)}$, $B_{11}^{(r)}$, $A_{30}^{(r)}$, $B_{30}^{(r)}$, respectively. Once these coefficients are calculated the limits of terms involving azimuthal and cross derivatives are also known using Eqs. (4) and (11), while streamwise derivatives of these coefficients are evaluated with the same scheme used for interior points. However, there is a more economical way to calculate these coefficients. Supposing that N_θ is divisible by 8, meaning that for every element in the series there is another situated exactly $\pi/4$ away, one can take advantage of the properties of $\sin(\theta)$ and $\cos(\theta)$ functions to evaluate the coefficients in Eqs. (17)–(19). For instance, using Eq. (17) for θ and $\theta + \pi/2$, one can obtain a system of two linear equations with two unknowns ($A_{10}^{(r)}$ and $B_{10}^{(r)}$):

$$\begin{aligned} u_r(\theta) &= A_{10}^{(r)} \cos(\theta) + B_{10}^{(r)} \sin(\theta), \\ u_r(\theta + \pi/2) &= -A_{10}^{(r)} \sin(\theta) + B_{10}^{(r)} \cos(\theta). \end{aligned} \tag{29}$$

To eliminate the bias toward a certain direction, one can solve the above system for every $\theta = (2\pi/N_\theta)(n - 1)$ with $n = 1$ to N_θ and average the results to get final values for $A_{10}^{(r)}$ and $B_{10}^{(r)}$. The same kind of treatment can be applied to determine $A_{01}^{(r)}$, $A_{20}^{(r)}$, $B_{20}^{(r)}$ by first getting the coefficient $A_{01}^{(r)}$ and then using Eq. (18) for θ and $\theta + \pi/4$ to calculate the remaining two coefficients. The coefficients involved in the expression for the second derivative of u_r can be determined more easily if we try to obtain at the same time the coefficients appearing in the expression for the second derivative of u_θ; i.e.,

$$\frac{\partial^2 u_\theta}{\partial r^2} = 2A_{11}^{(\theta)} \cos(\theta) + 2B_{11}^{(\theta)} \sin(\theta) + 2B_{30}^{(r)} \cos(3\theta) - 2A_{30}^{(r)} \sin(3\theta), \tag{30}$$

where use was made of Eq. (11). By writing Eqs. (19) and (30) at θ, $\theta + \pi/2$, $\theta + \pi/4$, $\theta + 3\pi/4$ and solving three systems of two linear equations, one can determinate the values of all coefficients similarly to the procedure employed above.

3. VALIDATION OF PROPOSED NUMERICAL ALGORITHM

The development of this new technique was driven by the interest of the authors in calculating the turbulence dynamics and acoustic radiation of turbulent compressible round jets using LES. This problem is especially relevant to the design of more effective jet engines with reduced noise emissions. The quality of the jet-noise predictions is determined by the accuracy (resolution) of the numerical method, and by the boundary condition (physical as well as numerical at the polar axis) treatment and the quality of the mesh. The general numerical method is described in detail in [18], while the details of the implementation of the dynamic LES model in the original DNS code can be found in [17].

The numerical method employs compact fourth- or sixth-order Pade schemes [20] for the spatial derivatives in the nonhomogeneous directions, and Fourier spectral methods in the homogeneous (azimuthal) direction. The number of modes is dropped near the polar axis so that the CFL constraint will be determined by the radial (or axial) spacing. No clustering of the points near $r = 0$ is needed. The solution is advanced in time using a four-step Runge–Kutta method. Zonal boundary conditions with artificial damping are employed near the inlet and outlet to absorb outgoing disturbances and to avoid spurious noise generation at these boundaries. Nonreflecting boundary conditions are used at the lateral boundary $r = R$, as well as damping terms in a layer close to this boundary.

Before discussing the laminar and LES simulations using different treatments at the centerline, it is important to validate the proposed centerline algorithm by considering a test case for which a theoretical solution exists and to investigate its effect on the expected order of accuracy of the numerical solution. An inviscid compressible circular jet at a Mach number $\mathrm{Ma} = U/c_\infty = 0.9$, with the mean velocity, density, and pressure distributions given by

$$\begin{aligned}
\bar{u}_x(r) &= U\left(0.5 - 0.5\tanh\left(\frac{0.25R_0}{h}(r/R_0 - R_0/r)\right)\right),\\
\bar{u}_r(r) &= 0,\\
\bar{u}_\theta(r) &= 0,\\
\bar{\rho}(r) &= \rho_\infty,\\
\bar{p}(r) &= 1/\gamma,
\end{aligned} \tag{31}$$

is forced at the fundamental frequency (temporal wavenumber) $\omega = 1.0278c_\infty/R_0$ and complex streamwise wavenumber $k = k_r + ik_i = (1.9275 - 0.6094i)(1/R_0)$ corresponding to $m = 1$ according to

$$q(x, r, \theta) = \bar{q}(r) + \zeta\,\mathrm{Real}\{(\hat{q}_r(r) + i\hat{q}_i(r))e^{i(kx+m\theta-\omega t)}\}, \tag{32}$$

where q is the instantaneous value of a generic variable, $\bar{q}$ is its mean value defined in (31), $\hat{q}_r$ and $\hat{q}_i$ are the real and imaginary parts of the scaled eigenvector associated with q, $\zeta = 10^{-4}$ is a chosen coefficient independent of the variable that determines the amplitude of the disturbances, R_0 is the initial radius of the jet in the inlet section, $h = 0.1R_0$ is the jet momentum thickness, c_∞ is the speed of sound at ambient conditions, and $\gamma = 1.4$ is the ratio of specific heats. All the eigenvectors are scaled with the maximum absolute value of the eigenvector associated with the streamwise velocity, so the value of ζ plays the role of amplification factor for the disturbances. The values of ω, k, and the form of the eigenvectors associated with u_x, u_r, u_θ, ρ, and p for $m = 1$ and the mean flow profiles given by (31) were determined from the inviscid linear stability theory using a shooting method.

The inlet boundary conditions in our calculations correspond to setting $x = 0$ in (32). The calculations were started from conditions identical to the theoretical solution (32) at $t = 0$. Given these initial and inflow boundary conditions, it is expected that during the initial phase of the jet development in the linear growth regime, the numerical solution should follow the theoretical solution if the maximum amplitude of the oscillations is small. As the radial and streamwise dimensions of our domain were $R = 6R_0$ and $X = 10R_0$, the maximum streamwise velocity disturbance in the exit section will be close to $\zeta e^{-k_i X} \sim 0.045 (U = 0.9)$. The subdomain that will be used to estimate the agreement between the simulations, and the theoretical solution has the dimensions $R = 3R_0$ and $X = 5R_0$. We verified that in this region, which does not contain any part of the lateral or exit damping regions, the growth of the disturbances is indeed governed by linear stability theory. The time step is $\Delta t = 0.001 R_0/U$, corresponding approximately to CFL $= 0.1$. The small value of the time step was chosen to eliminate as much as possible the temporal discretization errors for this model problem. Typically the code is run at CFL ~ 1.0.

The solutions corresponding to three simulations using three different grids containing $40 * 26 * 16$, $80 * 51 * 32$, and $160 * 101 * 64$ points in the (x, r, θ) directions are compared after $t = 12R_0/c_\infty$ (the period is $T = 2\pi/\omega = 6.11 R_0/c_\infty$). Each subsequent level of coarsening is obtained by the elimination of every other point in all three directions, starting from the finest mesh. The three grids have the characteristic grid size proportional to Δ_0, $\Delta_0/2$, and $\Delta_0/4$, where Δ_0 corresponds to the coarsest grid. The computed results show that the agreement between the numerical solution and the theoretical solution (32) improves significantly as the grid gets finer. This is illustrated in Fig. 1, where the distributions of the radial

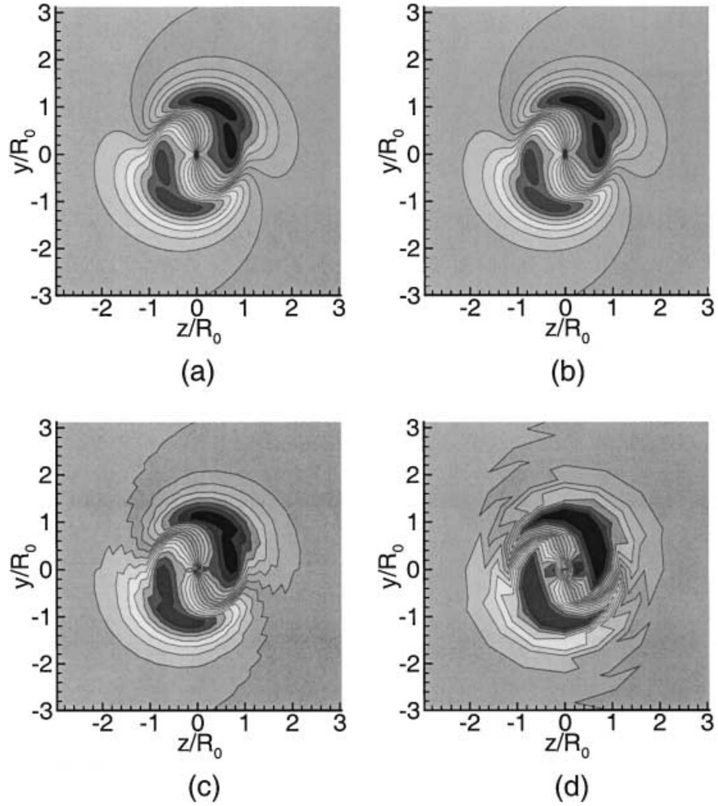

FIG. 1. Radial velocity contours in a plan situated at $x = 5R_0$ from the inlet section of the inviscid forced jet at time $t = 12R_0/U$. Radial velocity fields are shown with 15 equally spaced contours between $-0.0006U$ and $0.0006U$. (a) Theoretical solution via linear stability analysis; (b) fine-grid solution; (c) medium-grid solution; (d) coarse-grid solution.

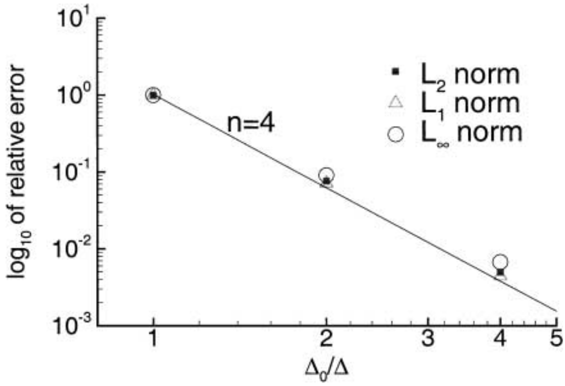

FIG. 2. Variation of error with mesh size for an inviscid test case.

velocity component in a plane situated at $x = 5R_0$ are shown for the theoretical solution and the fine-, medium-, and coarse-grid solutions. In particular, the agreement between the fine-grid solution and theoretical solution is excellent. A more quantitative assessment of the level of agreement between the calculated solution on a grid of size Δ and the theoretical solution can be obtained by looking at the error defined in the L_2, L_1, and L_∞ norms; i.e.,

$$e_\Delta^{(2)} = \sqrt{\frac{\sum_1^N (q_\Delta - q)^2}{N}}, \quad e_\Delta^{(1)} = \frac{\sum_1^N |q_\Delta - q|}{N}, \quad e_\Delta^{(\infty)} = \max|q_\Delta - q|, \tag{33}$$

where q_Δ is the calculated value, q is the theoretical value, and N is the number of points in the test volume ($0 < x < 5R_0$, $0 < r < 3R_0$, $0 < \theta < 2\pi$). The normalized error e_Δ (with respect to the coarse-grid results) for the streamwise velocity component is plotted in Fig. 2 in a log–log scale for the coarse, medium, and fine grids. As in these simulations fourth-order Pade schemes were used for the discretization of the spatial derivatives in the streamwise and radial directions, we assume that the error in the numerical solutions obtained on grids whose local grid size ratio is 2 should ideally scale as $2^n = 16$, where $n = 4$ is the expected order of accuracy. The slope corresponding to $n = 4$ is shown in Fig. 2 as a continuous line for comparison. One can see that, as expected, the slope of the error curve (which corresponds to the order of accuracy of the numerical solution) defined with either norm (see (33)) is close to 4. Also it is relevant to mention that if we do the same analysis for a much smaller volume around the centerline ($0 < r < 0.3R_0$) we obtain a very close result for the estimated order of accuracy of the numerical solution near the centerline. So, one can conclude that the errors near the centerline are not dominant.

In all the remaining calculations discussed here that correspond to laminar and turbulent jets, the Reynolds number is $\mathrm{Re} = U(2R_0)/\nu = 36{,}000$, the Mach number is $\mathrm{Ma} = 0.9$, and the computational grid consists of $192 * 128 * 64$ points in the (x, r, θ) directions, which is about an order of magnitude coarser than the grid used by Freund [16] to calculate a similar jet at $\mathrm{Re} = 3600$ using DNS. The mean flow distribution at the inlet plane is assumed to be a rounded top-hat profile with periodic disturbances in the streamwise direction. The simulations are run at a CFL number of one.

In a second test case (laminar forced jet) no randomized forcing is applied and the LES model is turned off. A sinusoidal perturbation at a Strouhal number $\mathrm{St} = 0.5$, corresponding

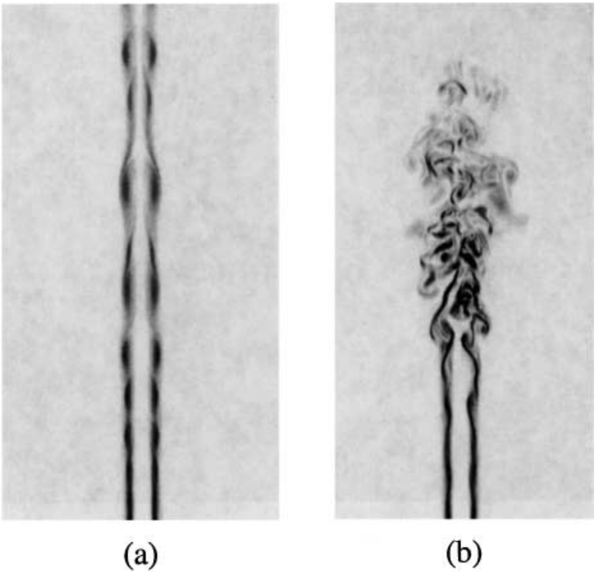

FIG. 3. Total vorticity contours. Vorticity shown using 18 equally spaced contours between 0 and $2U/R_0$. (a) Laminar forced jet; (b) turbulent jet.

to the most amplified wave, is imposed on the streamwise velocity profile. The forced-jet solution is quasiaxisymmetrical and laminar, as seen from the total vorticity contours in Fig. 3a. The effects of the different treatments at the polar axis are investigated in Fig. 4, where snapshots of the dilatation fields in the region $x > 20R_0$ are shown for different treatments at the polar axis. We choose the dilatation because this quantity is very sensitive to the centerline treatment and also provides relevant information for the jet acoustics in the near field. Case L1 corresponds to the method where the equations are solved in Cartesian coordinates, case L2 corresponds to a grid with no points placed at the polar axis (method described in [1]), and case L3 corresponds to the treatment using series expansions at the centerline. In the third test case randomized azimuthal forcing is applied in the input plane to trigger the three-dimensional instabilities for the LES calculation. All other parameters of the simulations, as well as the computational mesh, are kept the same as those used in the second test case. As seen in Fig. 3b the jet undergoes transition to turbulence at the end of

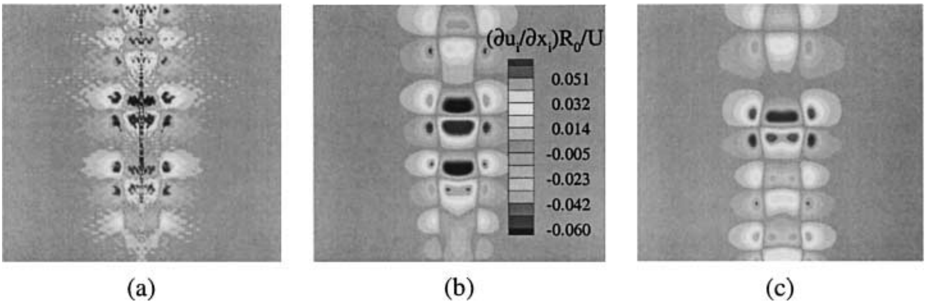

FIG. 4. Dilatation contours in the forced jet. (a) Cartesian coordinates; (b) method of Mohseni and Colonius; (c) series expansions treatment.

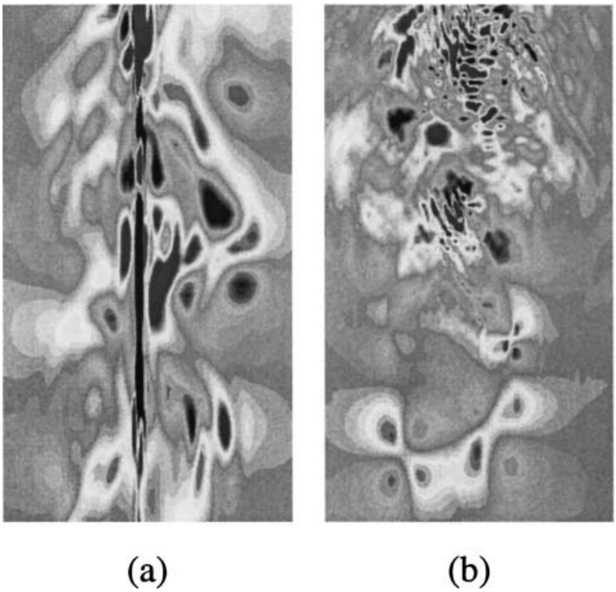

FIG. 5. Dilatation contours in an area situated after the end of the potential core for the turbulent jet. Dilatation fields are shown with 18 equally spaced contours between $-0.08U/R_0$ and $0.08U/R_0$. (a) Method of Mohseni and Colonius; (b) series expansions treatment.

the potential core situated around $x = 15R_0$. Results are shown in Fig. 5 for two simulations, the first (T1) uses the method of Mohseni and Colonius [1], while in the second (T2) the series expansion treatment is employed.

Considerable success was reported by Freund [16] for DNS simulations of jets at lower Reynolds numbers using the present numerical method with the equations at the centerline solved in Cartesian coordinates. As we are interested in simulating jets at very high Reynolds numbers (two to three orders of magnitude higher than the ones at which DNS is presently possible) the robustness of the method on coarser meshes is an obvious requirement. Our simulation showed that even for a laminar forced jet (case L1) strong oscillations in the dilatation field developed near the centerline in the form of two-delta waves. They are evident in Fig. 4a in the region near the polar axis, starting with the streamwise ($x \sim 15R_0$) location where ring vortices begin to be shed from the jet. These point-to-point oscillations in dilatation are on the order of $1.5R_0/U$, which is more than one order of magnitude higher that the values of $0.1R_0/U$ associated with the maximum dilatation inside the coherent structures of the jet. These problems were also apparent in the vorticity fields near the centerline. For case L1 the simulation did not diverge, but obviously the quality of the solution, especially the sound information that can be collected from these fields, is poor. When used to calculate a turbulent jet we were not able to get a well-behaved solution on the relatively coarse mesh used in these simulations without substantial filtering of the solution to remove the two-delta waves (every couple of time steps), and the quality of the solution was poor. This shows that the robustness of this polar axis treatment deteriorates rapidly on coarse meshes and for high Reynolds numbers, when strong nonlinear interactions are present in the flow. Several features of this method are suspected to be at the origin of the above-mentioned problems. First, the derivatives in the directions corresponding to the Cartesian coordinates are evaluated using six-order explicit central differences instead of sixth-order Pade schemes, while in the evaluation of the radial derivatives with compact differences, numerical boundary conditions using one-sided differences of lower order have to be formulated. Another source of errors may be associated with the bias introduced into the solution by the arbitrary choice ($N_\theta/2$ possibilities) of the two perpendicular directions after which the flow equations are solved at the centerline.

Both of these approximations are automatically removed when a staggered mesh in the radial direction is employed in simulation L2. However, our results using the technique proposed in [1] showed that in the absence of filtering, the solution would diverge after approximately 1000 time steps. That was due to a very local instability situated at the first point off the polar axis at a certain streamwise location. The dilatation field remained fairly smooth at all other streamwise locations close to the polar axis, in contrast to the results seen in case L1. However, when a sixth-order-accurate explicit filter ($\tilde{f} = (f_{i-3} - 6f_{i-2} + 15f_{i-1} + 44f_i + 15f_{i+1} - 6f_{i+2} + f_{i+3})/64$) was applied every 300 time steps to smooth the velocity field, the dilatation contours shown in Fig. 4b remained smooth and no unphysical oscillations were observed near the polar axis. The cutoff wavenumbers corresponding to values of the filtering transfer function of 0.9 and 0.5 are $\omega = 0.49\pi$ and $\omega = 0.71\pi$, respectively. Any of these values can be taken as representative for the cutoff wavenumber for the filter (see also [20] for more details about the filter properties). The behavior of the solution for the forced laminar jet seems to suggest that this method is not very robust for strong nonlinear problems, which would limit their use for turbulent calculations, especially on fairly coarse grids.

Finally, in case L3, where the new treatment using asymptotic series expansion was used at the polar axis, the dilatation fields are smooth (Fig. 4c) and the flow features are very similar to the results obtained with the method of Mohseni and Colonius, but no filtering was necessary to keep numerical instabilities from forming near the polar axis.

Based on the results from the second (laminar jet) test case, we focus our attention for turbulent calculations on the method proposed by Mohseni and Colonius [1] and on the method based on series expansions. Filtering the solution every 30 time steps, despite being sufficient for keeping the solution from diverging, does not remove the unphysical spurious oscillations in the dilatation field that are observed very close to the polar axis at all streamwise locations for $x > 15R_0$ (Fig. 5a). In fact the maximum values of the dilatation in these elongated structures very close to the polar axis are around $1.2R_0/U$, which is significantly higher than the levels of dilatation recorded in the rest of the computational domain. That is true even if the filter is applied more often. One should point out that this amount of filtering was found to have nonnegligible effects when sound sources were calculated from these fields. Thus, even though the method proposed in [1] gives comparable results with the series-expansions based technique for laminar forced jets, in turbulent simulations, the robustness and accuracy of the method in [1] appears to be inferior. The turbulent case is much more difficult to handle because the level of nonlinear flow interactions is much higher and jet structures are passing through the centerline. Convergence of the solution on relatively coarse meshes can be obtained in our simulations only by filtering the solution when the method of Mohseni and Colonius [1] is used.

In simulation T2, patches of high dilatation are observed in a region of about $10R_0$ in the streamwise direction, starting at the end of the inviscid core. The position of these patches is not very close to the polar axis (Fig. 5b), except when they are convected by the mean jet motion through the polar axis. The maximum absolute value of the dilatation field in the turbulent region is at all times around $0.2R_0/U$, including at the polar axis. The short waves that are seen at the top of Fig. 5b are rather related to the high-aspect ratio $\Delta x/\Delta r$ of the present grid and are not a consequence of centerline instabilities. Away from the centerline the dilatation field appears smoother in the case of T1 compared to that of T2, but this is just an effect due to the use of the filtering in T1. Even so, spurious waves or unrealistically high values of the dilatation (Fig. 5a, case T1) or vorticity at the first two to three points off the centerline are not observed.

The level of the unphysical spurious dilatation oscillations present in the domain close to the polar axis is greatly reduced compared to the case in which the method of Mohseni and Colonius [1] was used, while filtering was practically eliminated. The sixth-order explicit filter was applied every 500 time steps to eliminate the high-frequency waves that form because of the high grid-stretching ratio. Overall there is a significant increase in the robustness for the method using asymptotic series expansions compared to the other two approaches. Moreover, because we are primarily interested in extracting sound information from the near fields, elimination of filtering that may compromise substantially the quality of the sound data is a key factor in assessing the different methods.

4. SUMMARY

In this paper a general method for handling the singularities arising at the polar axis of the governing flow equations in cylindrical coordinates based on power series expansions in the radial direction and Fourier series in the azimuthal direction was presented. Using the most general form of these series expansions, we derived a new set of equations at the polar axis by calculating the limit of the various operators appearing in the governing system of equations (Eq. 1). The new method is computationally easy to implement and is less expensive than solving the equations in Cartesian coordinates at the centerline. The method was proven to be well defined in the sense that for any single-valued variable at the polar axis (scalar quantity or streamwise velocity) in the RHS of the Navier–Stokes equations only the $m = 0$ mode was shown to have a nonzero coefficient in the limit of $r \to 0$, despite the fact that individual terms had nonzero coefficients for modes ± 2 and ± 3. The momentum equations for u_r and u_θ are coupled in the limit $r \to 0$, and only modes $m = \pm 1$ are left in the RHS of the two momentum equations. Again, this is consistent with the asymptotic behavior of the radial and azimuthal velocities at the origin ($u_r(\theta + \pi/2) = u_\theta(\theta)$).

The present algorithm avoids the loss in accuracy at the centerline, where most of the finite-volume and finite-difference methods use some kind of one-sided differences to approximate the operators at the centerline. This is because in the context of the present method we were able to calculate the radial derivatives at the origin with the same order of accuracy as in the rest of the domain (fourth- or sixth-order compact differences) by using a domain mapping so that the points on the polar axis become regular interior points. As this is the only information needed to calculate the coefficients of the newly derived polar equations, there is no loss in the overall accuracy of the method. The coefficients in the asymptotic expansions are unique, so we do not have to choose any arbitrary directions, as is the case when the equations are solved in Cartesian coordinates at origin. One of the advantages is that the first point off the axis, where the various terms with singular behavior have to be evaluated, will be situated at Δr as opposed to $\Delta r/2$ (as is the case in the method of Mohseni and Colonius [1]), which may avoid an important source of errors or instabilities (e.g., due to the nonlinear interactions of eddies near the polar axis in a DNS or LES simulation).

The accuracy of the present centerline algorithm was tested for a simulation of a forced circular inviscid jet. The eigenvalues and eigenvectors of the mean jet velocity profile determined from inviscid linear stability theory were used to excite the inflow boundary of our jet. During the initial phases of the jet development the numerical solution should follow the theoretical solution for the forced jet in the linear growth regime. We were able to show that the numerical solutions converges toward the theoretical solution with increasing mesh density and that the accuracy of the overall calculation is not affected by the proposed centerline treatment; in other words, the spatial order of accuracy of the numerical solution is close to the order of the numerical method.

The robustness of the proposed approach was tested successfully by comparing results for a deterministically forced jet with similar calculations using the same numerical method but with the equations solved at the centerline in Cartesian coordinates, or without any points at $r = 0$ using the method described in [1]. Finally, the present technique was shown to give improved results over the method of Mohseni and Colonius [1] for the simulation of a compressible jet using LES on relatively coarse meshes, in which the flow interactions taking place near the polar axis are very important, and where a flow solution that is not contaminated by numerical artifacts originating at the singularity axis is required to accurately calculate the jet-noise sources.

One should point out that the algorithm presented here to deal with the polar axis singularities is not restricted to the use of the present numerical method, which uses Pade schemes to evaluate the derivatives in the radial and streamwise directions, or to solving the compressible flow equations. Rather it can be adapted in a straightforward way to handle the system of equations governing magnetohydrodynamics, combustion, and so forth. As spherical coordinates are locally cylindrical coordinates near the two singularity axes, the above method is also directly applicable to numerical methods that solve the flow equations in spherical coordinates. In this case the governing equations are different but the derivation of the set of equations valid at the two singularity axes is similar.

APPENDIX

The mass conservation, momentum, and equations for the compressible flow equations in cylindrical coordinates are

$$\frac{\partial \rho}{\partial t} = -\left(\frac{\partial \rho u_x}{\partial x} + \frac{1}{r}\frac{\partial r\rho u_r}{\partial r} + \frac{1}{r}\frac{\partial \rho u_\theta}{\partial \theta}\right), \tag{A1}$$

$$\frac{\partial \rho u_x}{\partial t} = -\left(\frac{\partial \rho u_x u_x}{\partial x} + \frac{1}{r}\frac{\partial r\rho u_x u_r}{\partial r} + \frac{1}{r}\frac{\partial \rho u_x u_\theta}{\partial \theta}\right) - \frac{\partial p}{\partial x} + V_x, \tag{A2}$$

$$\begin{aligned}\frac{\partial \rho u_r}{\partial t} &= -\left(\frac{\partial \rho u_r u_x}{\partial x} + \frac{1}{r}\frac{\partial r\rho u_r u_r}{\partial r} + \frac{1}{r}\frac{\partial \rho u_r u_\theta}{\partial \theta} - \frac{\rho u_\theta^2}{r}\right) - \frac{\partial p}{\partial r} + V_r,\\ \frac{\partial \rho u_\theta}{\partial t} &= -\left(\frac{\partial \rho u_\theta u_x}{\partial x} + \frac{1}{r}\frac{\partial r\rho u_\theta u_r}{\partial r} + \frac{1}{r}\frac{\partial \rho u_\theta u_\theta}{\partial \theta} + \frac{\rho u_r u_\theta}{r}\right) - \frac{1}{r}\frac{\partial p}{\partial \theta} + V_\theta,\end{aligned} \tag{A3}$$

$$\begin{aligned}\frac{\partial e}{\partial t} &= -\left(\frac{\partial (e+p)u_x}{\partial x} + \frac{1}{r}\frac{\partial r(e+p)u_r}{\partial r} + \frac{1}{r}\frac{\partial (e+p)u_\theta}{\partial \theta}\right)\\ &\quad + V_e + u_x V_x + u_r V_r + u_\theta V_\theta + \Psi.\end{aligned} \tag{A4}$$

The irreversible viscous dissipation, Ψ, is given by

$$\Psi = \tau_{xx}\frac{\partial u_x}{\partial x} + \tau_{xr}\frac{\partial u_r}{\partial x} + \tau_{x\theta}\frac{\partial u_\theta}{\partial x} + \tau_{xr}\frac{\partial u_x}{\partial r} + \tau_{rr}\frac{\partial u_r}{\partial r} + \tau_{\theta r}\frac{\partial u_\theta}{\partial r} + \frac{\tau_{x\theta}}{r}\frac{\partial u_x}{\partial \theta}$$
$$+ \frac{\tau_{r\theta}}{r}\frac{\partial u_r}{\partial \theta} + \frac{\tau_{\theta\theta}}{r}\frac{\partial u_\theta}{\partial \theta} + \frac{u_r\tau_{\theta\theta}}{r} - \frac{u_\theta\tau_{r\theta}}{r}. \tag{A5}$$

The viscous terms appearing in the momentum equations are

$$V_x = \frac{\partial \tau_{xx}}{\partial x} + \frac{1}{r}\frac{\partial r\tau_{xr}}{\partial r} + \frac{1}{r}\frac{\partial \tau_{x\theta}}{\partial \theta}, \tag{A6}$$

$$\begin{aligned} V_r &= \frac{\partial \tau_{xr}}{\partial x} + \frac{1}{r}\frac{\partial r\tau_{rr}}{\partial r} + \frac{1}{r}\frac{\partial \tau_{r\theta}}{\partial \theta} - \frac{\tau_{\theta\theta}}{r}, \\ V_\theta &= \frac{\partial \tau_{x\theta}}{\partial x} + \frac{1}{r}\frac{\partial r\tau_{\theta r}}{\partial r} + \frac{1}{r}\frac{\partial \tau_{\theta\theta}}{\partial \theta} + \frac{\tau_{r\theta}}{r}, \end{aligned} \tag{A7}$$

while the viscous flux term in the energy equation is

$$V_e = \frac{\partial}{\partial x}\left(\frac{\mu}{\Pr}\frac{\partial T}{\partial x}\right) + \frac{1}{r}\frac{\partial}{\partial r}\left(r\frac{\mu}{\Pr}\frac{\partial T}{\partial r}\right) + \frac{1}{r}\frac{\partial}{\partial \theta}\left(\frac{1}{r}\frac{\mu}{\Pr}\frac{\partial T}{\partial \theta}\right). \tag{A8}$$

In Eq. (A8) T is the temperature, Pr is the Prandtl number, and $\mu = \mu(T)$ is the shear viscosity. The viscous stresses in cylindrical coordinates are

$$\begin{aligned} \tau_{xx} &= \mu\left(2\frac{\partial u_x}{\partial x} + \Lambda\Theta\right), \\ \tau_{xr} &= \mu\left(\frac{\partial u_r}{\partial x} + \frac{\partial u_x}{\partial r}\right), \\ \tau_{x\theta} &= \mu\left(\frac{\partial u_\theta}{\partial x} + \frac{1}{r}\frac{\partial u_x}{\partial \theta}\right), \\ \tau_{rr} &= \mu\left(2\frac{\partial u_r}{\partial r} + \Lambda\Theta\right), \\ \tau_{r\theta} &= \mu\left(\frac{\partial u_\theta}{\partial r} + \frac{1}{r}\frac{\partial u_r}{\partial \theta} - \frac{u_\theta}{r}\right), \\ \tau_{\theta\theta} &= \mu\left(2\left(\frac{1}{r}\frac{\partial u_\theta}{\partial \theta} + \frac{u_r}{r}\right) + \Lambda\Theta\right). \end{aligned} \tag{A9}$$

The coefficient Λ in (A9) is defined as

$$\Lambda = \frac{\mu_B}{\mu} - \frac{2}{3}, \tag{A10}$$

where μ_B is the bulk viscosity ($\mu_B/\mu = 0.6$ for air according to [21]). The dilatation of the velocity field, Θ, is given by

$$\Theta = \frac{\partial u_x}{\partial x} + \frac{\partial u_r}{\partial_r} + \frac{1}{r}\left(u_r + \frac{\partial u_\theta}{\partial \theta}\right). \tag{A11}$$

In the following the series expansions coefficients introduced in Eq. (3) for a scalar variable s are $\alpha_{ij}^{(s)}$, $\beta_{ij}^{(s)}$ (for u_x, $s = x$; for ρu_x, $s = \rho x$), while those introduced in Eq. (4) for multi-valued variables (u_r, u_θ) are $A_{ij}^{(s)}$, $B_{ij}^{(s)}$, with $s = r$ and $s = \theta$. The derivative of the viscosity $\mu(T)$ is calculated as

$$\frac{\partial \mu}{\partial x_i} = \frac{\partial \mu}{\partial T}\frac{\partial T}{\partial x_i} = \eta(T)\frac{\partial T}{\partial x_i}. \tag{A12}$$

If the appropriate series expansions are introduced into Eqs. (A1) through (A8) and A(11) and the limit $r \to 0$ is taken, a new set of equations valid at the polar axis is obtained; i.e.,

$$\frac{\partial \rho}{\partial t} = -\left(\frac{\partial \alpha_{00}^{(\rho)}\alpha_{00}^{(x)}}{\partial x} + A_{10}^{(r)}\alpha_{10}^{(\rho)} + B_{10}^{(r)}\beta_{10}^{(\rho)} + 2A_{01}^{(r)}\alpha_{00}^{(\rho)}\right), \tag{B1}$$

$$\frac{\partial \rho u_x}{\partial t} = -\left(\frac{\partial \alpha_{00}^{(\rho x)}\alpha_{00}^{(x)}}{\partial x} + A_{10}^{(r)}\alpha_{10}^{(\rho x)} + B_{10}^{(r)}\beta_{10}^{(\rho x)} + 2A_{01}^{(r)}\alpha_{00}^{(\rho x)}\right) - \left(\frac{\partial \alpha_{00}^{(p)}}{\partial x}\right) + V_x, \tag{B2}$$

$$\begin{aligned}\frac{\partial \rho u_r}{\partial t} = -\Bigg(&\frac{\partial \alpha_{00}^{(\rho)}\alpha_{00}^{(x)}A_{10}^{(r)}}{\partial x}\cos(\theta) + \frac{\partial \alpha_{00}^{(\rho)}\alpha_{00}^{(x)}B_{10}^{(r)}}{\partial x}\sin(\theta) + \left(A_{10}^{(r)}\cos(\theta) + B_{10}^{(r)}\sin(\theta)\right)\\ &* \left(\alpha_{10}^{(\rho)}A_{10}^{(r)} + \beta_{10}^{(\rho)}B_{10}^{(r)}\right) + \alpha_{00}^{(\rho)}\big[3A_{01}^{(r)} * \left(A_{10}^{(r)}\cos(\theta) + B_{10}^{(r)}\sin(\theta)\right)\\ &- A_{01}^{(\theta)} * \left(B_{10}^{(r)}\cos(\theta) - A_{10}^{(r)}\sin(\theta)\right) + \cos(\theta) * \left(A_{10}^{(r)}A_{20}^{(r)} + B_{10}^{(r)}B_{20}^{(r)}\right)\\ &+ \sin(\theta) * \left(A_{10}^{(r)}B_{20}^{(r)} - B_{10}^{(r)}A_{20}^{(r)}\right)\big]\Bigg) - \left(\alpha_{10}^{(p)}\cos(\theta) + \beta_{10}^{(p)}\sin(\theta)\right) + V_r,\end{aligned} \tag{B3}$$

$$\begin{aligned}\frac{\partial e}{\partial t} = -\Bigg(&\frac{\partial \alpha_{00}^{(x)}\alpha_{00}^{(e+p)}}{\partial x} + A_{10}^{(r)}\alpha_{10}^{(e+p)} + B_{10}^{(r)}\beta_{10}^{(e+p)} + 2A_{01}^{(r)}\alpha_{00}^{(e+p)}\Bigg) + V_e + \alpha_{00}^{(x)}V_x\\ &+ A_{10}^{(r)}\frac{\partial}{\partial x}\left(\mu\left(\frac{\partial A_{10}^{(r)}}{\partial x} + \alpha_{10}^{(x)}\right)\right) + B_{10}^{(r)}\frac{\partial}{\partial x}\left(\mu\left(\frac{\partial B_{10}^{(r)}}{\partial x} + \beta_{10}^{(x)}\right)\right)\\ &+ \eta\Lambda\Theta\left(\alpha_{10}^{(T)}A_{10}^{(r)} + \beta_{10}^{(T)}B_{10}^{(r)}\right) + \mu\Lambda\left(\frac{\partial \alpha_{10}^{(x)}}{\partial x}A_{10}^{(r)} + \frac{\partial \beta_{10}^{(x)}}{\partial x}B_{10}^{(r)}\right)\\ &+ \mu\Lambda\left[\left(B_{11}^{(\theta)} + 3A_{11}^{(r)}\right)A_{10}^{(r)} + \left(3B_{11}^{(r)} - A_{11}^{(\theta)}\right)B_{10}^{(r)}\right]\\ &+ \mu\left[\left(5A_{11}^{(r)} - B_{11}^{(\theta)}\right)A_{10}^{(r)} + \left(5B_{11}^{(r)} + A_{11}^{(\theta)}\right)B_{10}^{(r)}\right] + 2\eta A_{01}^{(r)}\left(\alpha_{10}^{(T)}A_{10}^{(r)} + \beta_{10}^{(T)}B_{10}^{(r)}\right)\\ &+ 2\eta\left[\left(\alpha_{10}^{(T)}A_{20}^{(r)} + \beta_{10}^{(T)}B_{20}^{(r)}\right)A_{10}^{(r)} + \left(\alpha_{10}^{(T)}B_{20}^{(r)} - \beta_{10}^{(T)}A_{20}^{(r)}\right)B_{10}^{(r)}\right] + \Psi,\end{aligned} \tag{B4}$$

$$\begin{aligned}\Psi = \mu&\frac{\partial \alpha_{00}^{(x)}}{\partial x}\left(2\frac{\partial \alpha_{00}^{(x)}}{\partial x} + \Lambda\Theta\right) + 2\mu\Lambda\Theta A_{01}^{(r)} + 4\mu\left(A_{01}^{(r)}A_{01}^{(r)} + A_{20}^{(r)}A_{20}^{(r)} + B_{20}^{(r)}B_{20}^{(r)}\right)\\ &+ \mu\left[\frac{\partial A_{10}^{(r)}}{\partial x}\frac{\partial A_{10}^{(r)}}{\partial x} + \frac{\partial B_{10}^{(r)}}{\partial x}\frac{\partial B_{10}^{(r)}}{\partial x} + 2\alpha_{10}^{(x)}\frac{\partial A_{10}^{(r)}}{\partial x} + 2\beta_{10}^{(x)}\frac{\partial B_{10}^{(r)}}{\partial x} + \alpha_{10}^{(x)}\alpha_{10}^{(x)} + \beta_{10}^{(x)}\beta_{10}^{(x)}\right],\end{aligned} \tag{B5}$$

$$\begin{aligned}V_x = &\frac{\partial}{\partial x}\left(\mu\left(2\frac{\partial \alpha_{00}^{(x)}}{\partial x} + \Lambda\Theta\right)\right) + \mu\left(4\alpha_{01}^{(x)} + 2\frac{\partial A_{01}^{(r)}}{\partial x}\right)\\ &+ \eta\cdot\left(\alpha_{10}^{(T)}\frac{\partial A_{10}^{(r)}}{\partial x} + \beta_{10}^{(T)}\frac{\partial B_{10}^{(r)}}{\partial x} + \alpha_{10}^{(T)}\alpha_{10}^{(x)} + \beta_{10}^{(T)}\beta_{10}^{(x)}\right),\end{aligned} \tag{B6}$$

$$\begin{aligned} V_r = {} & \cos(\theta)\frac{\partial}{\partial x}\left(\mu\cdot\left(\frac{\partial A_{10}^{(r)}}{\partial x}+\alpha_{10}^{(x)}\right)\right)+\sin(\theta)\frac{\partial}{\partial x}\left(\mu\cdot\left(\frac{\partial B_{10}^{(r)}}{\partial x}+\beta_{10}^{(x)}\right)\right) \\ & +\eta\Lambda\Theta\left(\alpha_{10}^{(T)}\cos(\theta)+\beta_{10}^{(T)}\sin(\theta)\right)+\mu\Lambda\left(\frac{\partial\alpha_{10}^{(x)}}{\partial x}\cos(\theta)+\frac{\partial\beta_{10}^{(x)}}{\partial x}\sin(\theta)\right) \\ & +\mu\Lambda\left[\left(B_{11}^{(\theta)}+3A_{11}^{(r)}\right)\cos(\theta)+\left(3B_{11}^{(r)}-A_{11}^{(\theta)}\right)\sin(\theta)\right]+\mu\left(\left(5A_{11}^{(r)}-B_{11}^{(\theta)}\right)\cos(\theta)\right. \\ & \left.+\left(A_{11}^{(\theta)}+5B_{11}^{(r)}\right)\sin(\theta)\right)+2\eta\left[A_{01}^{(r)}\left(\alpha_{10}^{(T)}\cos(\theta)+\beta_{10}^{(T)}\sin(\theta)\right)\right] \\ & +2\eta\left[\left(\alpha_{10}^{(T)}A_{20}^{(r)}+\beta_{10}^{(T)}B_{20}^{(r)}\right)\cos(\theta)+\left(\alpha_{10}^{(T)}B_{20}^{(r)}-\beta_{10}^{(T)}A_{20}^{(r)}\right)\sin(\theta)\right], \end{aligned} \tag{B7}$$

$$V_e=\frac{\partial}{\partial x}\left(\frac{\mu}{\mathrm{Pr}}\frac{\partial\alpha_{00}^{(T)}}{\partial x}\right)+4\frac{\mu}{\mathrm{Pr}}\alpha_{01}^{(T)}+\frac{\eta}{\mathrm{Pr}}\left(\alpha_{10}^{(T)}\alpha_{10}^{(T)}+\beta_{10}^{(T)}\beta_{10}^{(T)}\right), \tag{B8}$$

$$\Theta=\frac{\partial\alpha_{00}^{(x)}}{\partial x}+2A_{01}^{(r)}. \tag{B9}$$

In deducing the final form of Eqs. (B1) through (B8) repeated use was made of Eq. (11). Equations (B3) and (B7) were obtained by using the expressions for the radial momentum equations and its viscous term (the first equation in (A3) and (A7)). As we pointed out in the paper the expressions obtained using the azimuthal momentum equation and its corresponding viscous term (the third equation in (A3) and (A7)) are redundant in the sense that the two independent equations corresponding to the $m = 1$ and $m = -1$ modes will be exactly the same as the ones deduced using only the expressions of the radial momentum equation and its viscous term. Nevertheless, if this method is applied to another system of equations, doing the calculations for both the radial and azimuthal directions may serve as a check of the calculation. For the LES simulations there are additional terms arising from the subgrid-scale modeling. For instance, the new term in the energy equation is

$$V_{\mathrm{SGS}}=\frac{\partial}{\partial x}\left(\vartheta\frac{\partial T}{\partial x}\right)+\frac{1}{r}\frac{\partial}{\partial r}\left(\vartheta r\frac{\partial T}{\partial r}\right)+\frac{1}{r}\frac{\partial}{\partial\theta}\left(\vartheta\frac{1}{r}\frac{\partial T}{\partial\theta}\right), \tag{A13}$$

where $\vartheta = \rho\nu_t/\mathrm{Pr}_t$, ν_t is the eddy viscosity, and Pr_t is the turbulent Prandtl number. As ϑ is a function of space that cannot be related directly to the temperature, as was μ, series expansions should be used for this coefficient when the limit is taken in Eq. (A13). The final form will be

$$V_{\mathrm{SGS}}=\frac{\partial}{\partial x}\left(\alpha_{00}^{(\vartheta)}\frac{\partial\alpha_{00}^{(T)}}{\partial x}\right)+4\alpha_{00}^{(\vartheta)}\alpha_{01}^{(T)}+\left(\alpha_{10}^{(\vartheta)}\alpha_{10}^{(T)}+\beta_{10}^{(\vartheta)}\beta_{10}^{(T)}\right). \tag{B10}$$

Note that ϑ is evaluated directly in physical space using Lilly's contraction in the present implementation of the dynamical model (as opposed of calculating first Pr_t), and its series expansion is calculated in the same way as for the eddy viscosity ν_t.

ACKNOWLEDGMENT

This work was supported in part by Grant NA G2-1373 from the NASA Ames Research Center.

REFERENCES

1. K. Mohseni and T. Colonius, Numerical treatment of polar coordinate singularities, *J. Comput. Phys.* **157**, 787 (2000).
2. M. D. Griffin, E. Jones, and J. D. Anderson, A computational fluid dynamic technique valid at the centerline for non-axisymmetric problems in cylindrical coordinates, *J. Comput. Phys.* **30**, 352 (1979).
3. P. L. O'Sullivan and K. S. Breuer, Transient growth in circular pipe flow. I. Linear disturbances, *Phys. Fluids* **6**(11), 3643 (1994).
4. S. A. Orszag and A. T. Patera, Secondary instability of wall-bounded shear flows, *J. Fluid Mech.* **128**, 347 (1983).
5. Y. Zhang, A. Gandgi, A. G. Tomboulides, and S. A. Orszag, Simulation of pipe flow, in *Symposium on Application of Direct and Large Eddy Simulation to Transition and Turbulence* (AGARD Conf., Crete, Greece, 1994). Vol. CP-551, pp. 17.1–17.9.
6. P. Loulou, *Direct Numerical Simulation of Incompressible Flow Using a B-Spline Spectral Method*, Ph.D. thesis (Department of Aeronautics and Astronautics, Stanford University, 1996).
7. A. G. Tomboulides, S. A. Orszag, and G. E. Karniadakis, *Direct and Large-Eddy Simulations of Axisymmetric Wakes*, AIAA Paper 93-0546 (1993).
8. W. Huang and D. M. Sloan, Pole condition for singular problems: The pseudospectral approximation, *J. Comput. Phys.* **107**, 254 (1993).
9. J. C. M. Eggels, F. Unger, M. H. Weiss, J. Westerweel, R. J. Adrian, R. Friedrich, and F. T. M. Nieuwstadt, Fully developed turbulent pipe flow: A comparison between direct numerical simulation and experiment, *J. Fluid Mech.* **268**, 175 (1994).
10. K. Akselvoll and P. Moin, *Large Eddy Simulation of Turbulent Confined Coannular Jets and Turbulent Flow over a Backward Facing Step*, Report TF-63 (Department of Mechanical Engineering, Stanford University, 1995).
11. K. Akselvoll and P. Moin, An efficient method for temporal integration of the Navier–Stokes equations in confined axisymmetric geometries, *J. Comput. Phys.* **125**, 454 (1996).
12. B. J. Boersma, G. Brethouwer, and F. T. M. Nieuwstadt, A numerical investigation on the effect of the flow conditions on the self-similar region of a round jet, *Phys. Fluids* **10**(4), 899 (1998).
13. R. Verzicco and P. Orlandi, A finite-difference scheme for three-dimensional incompressible flows in cylindrical coordinates, *J. Comput. Phys.* **123**, 402 (1996).
14. P. Orlandi and M. Fatica, Direct simulations of turbulent flow in a pipe rotating about its axis, *J. Fluid Mech.* **343**, 43 (1997).
15. B. E. Mitchell, S. K. Lele, and P. Moin, Direct computation of the sound generated by an axisymmetric jet, *AIAA J.* **35**(10), 1574 (1997).
16. J. B. Freund, *Acoustic Sources in a Turbulent Jet: A Direct Numerical Simulation Study*, AIAA Paper 99-1858 (1999).
17. B. J. Boersma and S. K. Lele, Large eddy simulation of compressible turbulent jets, in *Center for Turbulence Research Annual Research Briefs* (Dept. of Mechanical Engineering, Stanford Univ., Stanford, CA, 1999), pp. 365–374.
18. J. B. Freund, P. Moin, and S. K. Lele, *Compressibility Effects in a Turbulent Annular Mixing Layer*, Report TF-72 (Department of Mechanical Engineering, Stanford University, 1997).
19. J. P. Boyd, *Chebyshev and Fourier Spectral Methods* (Springler-Verlag, Berlin/Heidelberg, 1989).
20. S. K. Lele, Compact finite difference schemes with spectral-like resolution, *J. Comput. Phys.* **103**, 16 (1992).
21. P. A. Thompson, *Compressible Fluid Dynamics* (McGraw–Hill, New York, 1991).